

FULL PAPER

Open Access



# Light ion dynamics in the topside ionosphere and plasmasphere during geomagnetic storms

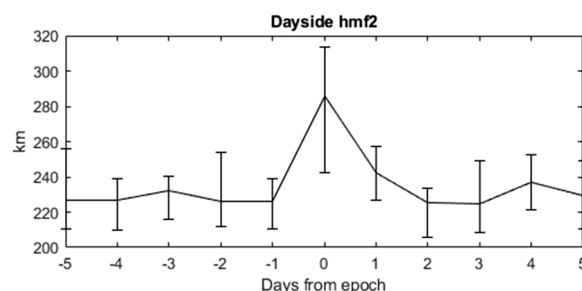
I. P. Pakhotin<sup>1\*</sup> , J. K. Burchill<sup>1</sup>, M. Förster<sup>2,3</sup> and L. Lomidze<sup>1</sup>

## Abstract

Storm-time topside ionosphere plasma composition, especially the light ion fraction, is an important parameter which controls magnetosphere–ionosphere coupling, plays a part in the growth of local instabilities, and provides information about the ring current, ion upflow, movement of ionization and other important physical processes and parameters. Ion composition is difficult to estimate on fine scales as empirical models tend to be parametrized by fixed inputs, ignoring the role of memory in plasma, and to preferentially capture large scales, while ground radars have limited coverage. In particular, ionospheric composition measurements at mid-latitude are lacking. Here we show, using the new Swarm SLIDEM effective ion mass measurement, a superposed epoch analysis of storm-time dayside and nightside effective ion mass changes, demonstrating the extent and timescales of motion of the [O<sup>+</sup>]/[H<sup>+</sup>] transition height with the main phase of geomagnetic storms, as well as directly observing evidence for the latitude dependence of these dynamics.

**Keywords** Plasma density, Ionospheric composition, Ionospheric convection, Langmuir probe, Ionosphere, Space weather

## Graphical Abstract



\*Correspondence:

I. P. Pakhotin

i.p.pakhotin@gmail.com

<sup>1</sup> Department of Physics and Astronomy, University of Calgary, Calgary, AB, Canada

<sup>2</sup> German Research Centre for Geosciences, Helmholtz Centre Potsdam, Potsdam, Germany

<sup>3</sup> Max Planck Institute for Solar System Research, 37077 Göttingen, Germany



© The Author(s) 2023. **Open Access** This article is licensed under a Creative Commons Attribution 4.0 International License, which permits use, sharing, adaptation, distribution and reproduction in any medium or format, as long as you give appropriate credit to the original author(s) and the source, provide a link to the Creative Commons licence, and indicate if changes were made. The images or other third party material in this article are included in the article's Creative Commons licence, unless indicated otherwise in a credit line to the material. If material is not included in the article's Creative Commons licence and your intended use is not permitted by statutory regulation or exceeds the permitted use, you will need to obtain permission directly from the copyright holder. To view a copy of this licence, visit <http://creativecommons.org/licenses/by/4.0/>.

## Introduction

The plasma composition of the topside ionosphere (above the F-region peak) and its response to space weather form a key part of several significant magnetosphere–ionosphere–thermosphere (MIT) coupling processes. Storm-time plasmasphere erosion and refilling (e.g., Carpenter and Lemaire 1997; Gallagher et al. 2021), ion outflow (Yau and André 1997), species-dependent ring current evolution (e.g., Chappell 1982; Nosé et al. 2020), vertical motion of the F-layer peak (e.g., Rishbeth et al. 1987; Rishbeth 1998), equatorial ion fountain (e.g., Balan et al. 2018), etc., all impact the relative composition of ionospheric plasma. In turn, understanding the plasma composition and its dynamics allows to construct more accurate maps of species density profiles, estimate characteristic timescales for significant events, and potentially infer more accurately the degree of electromagnetic coupling between the subsystems. Besides the so-called transition height (i.e., the altitude where  $[O^+] = [H^+]$ ), the balance of light and heavy (primarily  $O^+$ ) ions determines the Alfvén speed which is an important parameter in MIT coupling through its relationship with integrated Pedersen conductance to form the reflection coefficient governing downwards Poynting flux (Lysak 1991; Knudsen et al. 1992; Pakhotin et al. 2018, 2020, 2021; Billett et al. 2022). In addition, the propagation of magnetospheric plasma waves such as electromagnetic ion cyclotron (EMIC) waves, which play a significant role in radiation belt dynamics (e.g., Shprits et al. 2008), is governed by the relative abundances of ion species. As such, the inner magnetosphere abundances of these constituent species will govern the strength and location of phenomena such as Buchsbaum resonances (Buchsbaum 1960) which significantly affect propagation pathways of these important instabilities (Kim and Johnson 2016; Pakhotin et al. 2022b). Not least, the presence of light ions has implications for density estimations through Langmuir probes (Xiong et al. 2022; Park 2022; Pakhotin et al. 2022a, b), when, for example, assumptions are made as to the ion composition (Knudsen et al. 2017). In all, the constituent ion composition of topside ionospheric plasma is an important parameter and the ability to measure or estimate light ion abundances at high spatio-temporal resolution helps significantly in ionospheric and inner magnetospheric studies.

Unfortunately, plasma composition is not easy to measure. Using mass spectrometry may result in the lowest-energy particles being missed through not having enough energy to reach the detector. It is possible to estimate relative ion abundances from ion velocity measurements, as on CNOFS/CINDI and e-POP IRM (Yau and James 2015). However, CNOFS was in an equatorial orbit and could not obtain measurements at mid-to-high

latitudes, while e-POP's IRM coverage is sporadic and care is required in interpreting IRM data to obtain reliable physical measurements (Hussain and Marchand 2014; Marchand and Hussain 2015). It is also possible to obtain the  $H^+$  fraction from ground radars, e.g., Jicamarca and Kharkiv (e.g., Kotov et al. 2018). In particular, Kotov et al. (2019) and Reznichenko (2021) used the Kharkiv radar to analyze the motion of the F2 layer peak altitude ( $hmF2$ ) with space weather influences and were able to track the changes in the  $H^+$  fraction with height. These ground radars, however, are fixed in space and thus cannot observe a range of latitudes.

It is also possible to use empirical models such as TBT-2015 (Truhlik et al. 2015) which is incorporated into the International Reference Ionosphere (Bilitza et al. 2017; Bilitza and Xiong 2021). However, these ion composition models may not accurately reflect the dynamics occurring in a real ionosphere with memory. In particular, TBT-2015 is driven by the daily F10.7 index, which cannot track the rapid changes in ion composition that occur during storms on timescales of hours. The estimates for the ion composition can also be obtained from the physics-based models, however the accuracy of their results strongly depends on the empirical model inputs such as neutral density and winds (e.g., Krall et al. 2016).

In this study, we use the new Swarm SLIDEM data product (Pakhotin et al. 2022a), which includes an improved measure of plasma density (compared with the standard Swarm L1b ion density data product), as well as effective ion mass, which is a sensitive measure of the relative abundance of light ions in the ambient plasma. The study uses a superposed epoch analysis to study storms with a Dst index minimum of below  $-50$  nT. We observe the changes in effective ion mass in the 5 days before and after each storm, which reflects considerable ion mass composition changes in that range. We demonstrate day-side and night-side statistics for changes in effective ion mass and ion density. The ion composition changes are believed to be due to storm-time vertical transport of the topside ionosphere, and we corroborate this with measurements from ground-based ionosondes.

## Data and methodology

### The swarm SLIDEM dataset

The European Space Agency Swarm mission (Friis-Christensen et al. 2008) consists of 3 identical satellites launched in 2013 into a low-Earth polar orbit, with Swarm A and C flying side by side at heights of  $\sim 450$  km, while Swarm B is higher at  $\sim 520$  km. The satellites carry Electric Field Instruments or EFI (Knudsen et al. 2017), which comprise the Thermal Ion Imagers (TII) and Langmuir Probes (LP). The TII provides cross-track ion drifts at 16 Hz while the LP provides spherical probe

measurements at 2 Hz and EFI faceplate current measurements at 16 Hz. Recently, the Swarm SLIDEM product was developed (Pakhotin et al. 2022a), which utilizes current measurements obtained from the EFI faceplate and combines them with ion harmonic mode readings from the Langmuir probe to obtain more accurate measurements of plasma density, effective ion mass (at latitudes below 50 deg quasi-dipole latitude, or QDlat) and along-track ion drift velocity (above 50 deg QDlat). The effective ion mass  $M_{\text{eff}}$  is defined by:

$$\frac{1}{M_{\text{eff}}} = \frac{1}{N_i} \sum_{s=1}^k N_s \frac{1}{m_s}, \quad (1)$$

where  $m_s$  and  $N_s$  is the mass and density of the  $s$ th ion species (H<sup>+</sup>, O<sup>+</sup>, He<sup>+</sup>, N<sup>+</sup>, any molecular ions, etc.), and  $N_i$  is the total ion density (summed over all  $N_s$ ).  $M_{\text{eff}}$  is also known as reduced ion mass. A feature of Eq. (1) is that it is very sensitive to small variations in light ions. For example, an increase in H<sup>+</sup> fraction from 0% H<sup>+</sup> and 100% O<sup>+</sup>, to 10% H<sup>+</sup> and 90% O<sup>+</sup>, will lead  $M_{\text{eff}}$  to drop from 16 to 6.4 Atomic Mass Units (AMU). As such, it is a sensitive light ion detector which, unlike some spectrometry-based methods, responds to all ions, including cold plasma characterized by temperatures much less than 1 eV.

The methodology is a superposed epoch analysis across 4 years of data (2016–2020) for the three Swarm satellites. For this time period, the Dst index was obtained from NASA OMNIWeb (King and Papitashvili 2005), and filtered by including excursions below −50 nT. For each excursion, the time of minimum Dst formed the ‘zero epoch’, and for the 5 days before and after the zero epoch,

effective ion mass and density time series were obtained for the dayside and the nightside. Figure 1 shows the Swarm C SLIDEM effective ion mass estimate as a function of time and QDlat argument of orbit for an example event, where for the descending orbit (the nightside during the time period of Fig. 1), the quasi-dipole latitude is flipped and shifted by +180 degrees. In this way, −90 to 0 deg is the south hemisphere on the ascending track, 0 to +90 deg is the north hemisphere on the ascending track, +90 to +180 deg is the north hemisphere on the descending track, and +180 to +270 deg is the south hemisphere on the descending track. Dashed lines denote the ±50 deg QDlat boundaries beyond which the effective mass estimate is expected to be unreliable due to the presence of along-track auroral-zone ion drifts. Only effective ion mass estimates equatorward of ±50 deg QDlat are considered in this analysis.

In Fig. 1a, a rapid rise in effective ion mass is seen during the storm main phase during 30 August–1 September 2019, signifying increased [O<sup>+</sup>] fraction, which begins to return to pre-storm values ~2–3 days after the Dst minimum. As noted, the TBT-2015 model (Truhlik et al. 2015), plotted in Fig. 1b, fails to capture the  $M_{\text{eff}}$  changes as it is driven by the daily F10.7 index and does not capture storm-time changes on the timescale of hours.

In our analysis to study the response of SLIDEM data to the geomagnetic storms, an average of the effective ion mass is obtained for each time 2.4-h time bin, across the whole ±50 deg QDlat range. This analysis is repeated for each storm (<−50 nT Dst) and the superposed epoch statistics are calculated with median values, as well as the 25% and 75% quartiles. The same analysis is also repeated for SLIDEM density, which is taken across the

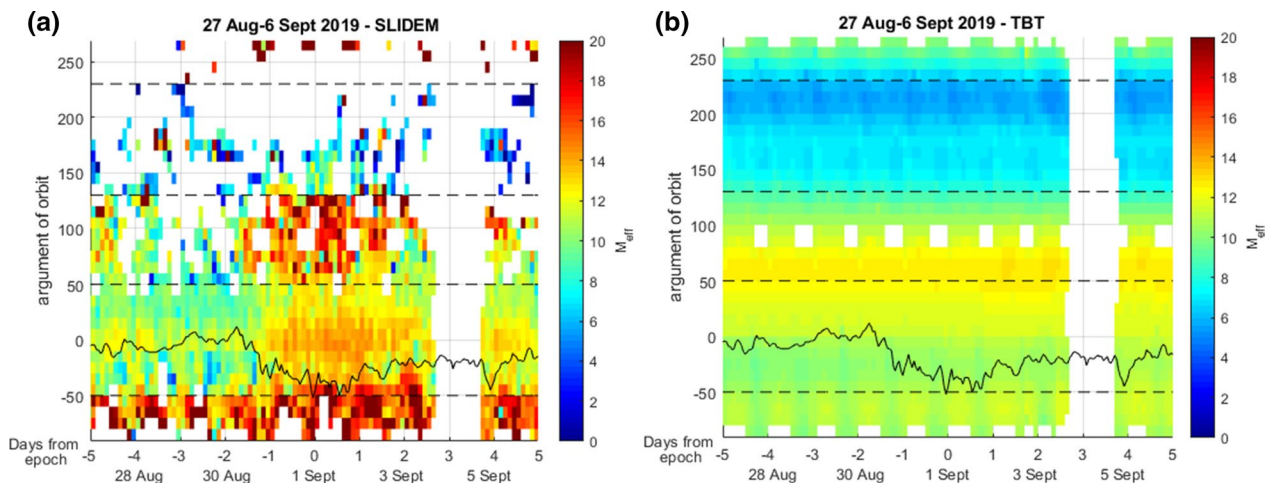


**Fig. 1** a SLIDEM effective ion mass plot for a sample time period (Dst minimum on 1 Sept 2019), with the Dst index overplotted as a black curve; **b** shows the same but for the TBT-2015 model. Dayside is in the bottom half of the plot, nightside in the top half. Ascending MLT = 12.5, descending MLT = 0.5

entire range  $\pm 90$  deg QDlat for dayside and 90–270 deg QDlat for nightside. Unlike effective ion mass, SLIDEM ion density estimates are generally valid for all latitudes.

It should be noted that occasionally,  $M_{\text{eff}}$  values of  $> 16$  AMU are observed in SLIDEM data. It is not clear whether these are of physical origin, signifying the presence of molecular ions, or of instrumental origin; further discussion may be found in Pakhotin et al. (2022a, b). The overall measured diurnal trends agree well with the empirical model albeit with larger amplitudes that may be related to calibration of the technique. We therefore retain  $M_{\text{eff}}$  values of  $> 16$  AMU in the technical analysis.

### Conjunctions with ionosondes

In order to obtain independent confirmation of the nature of the storm-time dynamics inferred from the Swarm SLIDEM product, data from ground-based ionosondes were utilized. The ionosonde data were obtained from the Digital Ionosonde Database (Reinisch and Galkin 2011) which comprises data for 2016–2020 from a network of ionosonde stations across the world. For this study, the maximum F2-layer height (HmF2) and the F2 critical frequency ( $f_0F2$ ) are utilized. The maximum F2-layer density (NmF2) may be obtained from the critical frequency (e.g., Ezquer et al. 2011) using:

$$N_mF2 = 1.24e10 \times f_0F2^2, \quad (2)$$

where  $N_mF2$  is in  $\text{m}^{-3}$  and  $f_0F2$  is in MHz.

### Results

The statistics for Swarm A and C, as well as Swarm B, superposed epoch results for dayside effective ion mass and density are displayed in Fig. 2 (the upper and lower error bars represent the 75% and 25% quartiles, respectively). It can be seen that Swarm A and C results are largely self-similar, although Swarm C displays less variation of  $M_{\text{eff}}$  and has more stable quartile ranges over the temporal development. This is primarily believed to be due to the greater availability of SLIDEM results for Swarm C, because SLIDEM requires the TII faceplate to be biased at  $-3.5$  V, which precludes the operation of TII in its main role to collect ion velocity measurements, during which the faceplate bias is  $-1.0$  V. Since ion velocity measurements are more often collected on Swarm A, on Swarm C the TII faceplate is more often run at  $-3.5$  V. In fact, for the year 2019, Swarm C has an almost continuous coverage for the SLIDEM product. Another difference in Fig. 2 is that  $M_{\text{eff}}$  on Swarm A appears to be somewhat larger, by  $\sim 1$  AMU. This may be due to instrumental differences which have not been accounted for by the SLIDEM processor. Finally, inter-quartile ranges

become more focused around the time corresponding to the maximum  $M_{\text{eff}}$  value, which is best seen for Swarm B.

In the days preceding the storm, for Swarm A and C the effective ion mass was  $\sim 14$ – $15$  AMU on the dayside. After the beginning of the storm and during the main phase, the effective ion mass rises rapidly in the course of several hours to  $\sim 15.5$ – $16$  AMU, suggesting almost 100% O $^{+}$ . After the main phase storm minimum,  $M_{\text{eff}}$  declines to pre-storm levels over the course of the next several days. The same dynamics are observed with the higher-orbiting Swarm B (Fig. 2e, f), but the  $M_{\text{eff}}$  values there rise from  $\sim 12.5$  AMU to  $\sim 15$  AMU, signifying larger light ion (most likely predominantly H $^{+}$ ) abundances at the higher orbit. Interestingly, unlike  $M_{\text{eff}}$ , the density data (Fig. 2b, d, f) do not show such clear variation, although all 3 Swarm satellites do observe minor dayside density enhancements around the time of the main phase, and the upper quartiles also feature secondary density maxima around 1–1.5 days after zero epoch, which is not seen on the nightside (Fig. 3). In all, the three satellites observe dayside increases in  $M_{\text{eff}}$  within several hours preceding the Dst index minimum, which continues for several hours after the Dst minimum and is followed by a slower ‘recovery’ to pre-storm values over the next several days. In fact, the  $M_{\text{eff}}$  dynamics closely mirror the Dst index dynamics, which is not the case for density. The ion and electron temperature estimates using SITE (Lomidze et al. 2021), displayed in Additional file 1: Fig. S1, also show no significant changes with the Dst index.

The same analysis has been performed for the nightside, with the results displayed in Fig. 3. It can be seen that, in general for  $M_{\text{eff}}$ , the same dynamics are observed, with a rapid increase in  $M_{\text{eff}}$  beginning in the hours preceding minimum Dst, and with  $M_{\text{eff}}$  reaching its peak values several hours after the Dst minimum. On the nightside, Swarm A and C observe increases in nighttime  $M_{\text{eff}}$  from  $\sim 9$  AMU to  $\sim 13$  AMU, while for Swarm B  $M_{\text{eff}}$  rises from  $\sim 6$  to  $\sim 11$  AMU. These  $M_{\text{eff}}$  values are lower than dayside  $M_{\text{eff}}$ , in line with expectations of greater nightside [H $^{+}$ ] abundances. Interestingly, the storm-time density enhancements are less pronounced for Swarm A and C, and more noticeable for Swarm B.

In order to corroborate the observed Swarm results, ground-based ionosonde data were utilized to independently analyze hmF2 and NmF2 changes with storm times. For each of the 39 identified storms, the Dst minimum (employing the zero epoch methodology as for Swarm), the date and nearest hour were identified. Then, for that date and hour, ionosonde stations were identified, comprising the closest station to local time noon (12 LT) and local midnight (00 LT). For example, if the Dst minimum occurred close to 08 UTC, a suitable ionosonde station observing local midnight



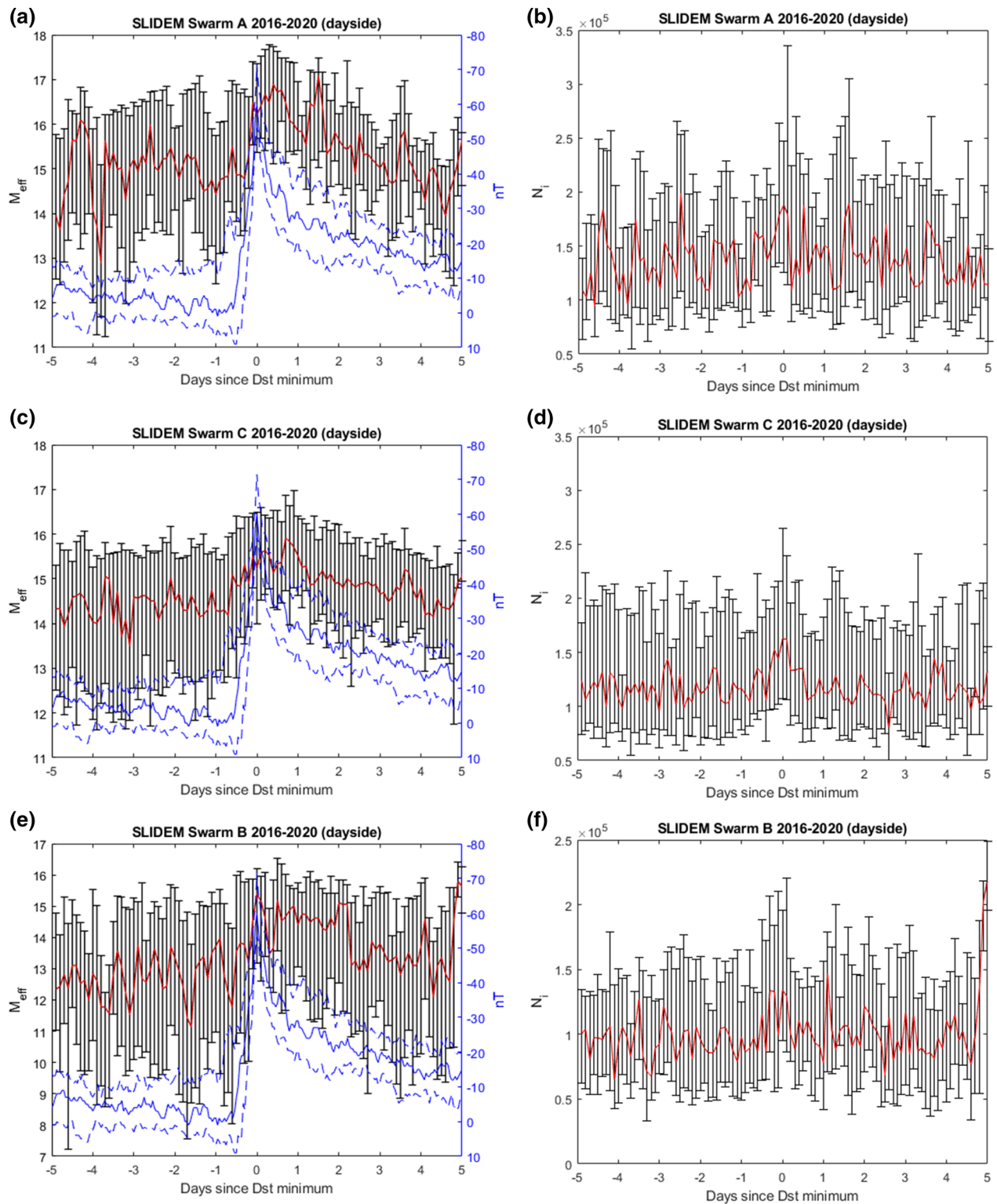


**Fig. 2** Superposed epoch analysis of dayside effective ion mass (left) and density (right) for Swarm A (top), C (middle) and B (bottom), for the years specified in the panel titles. **a**, **c** and **e** show the effective ion mass for Swarm A, Swarm C and Swarm B respectively, while **b**, **d** and **f** show the ion density for the same spacecraft. The plots show the median values (red), while error bars denote the upper and lower quartiles. Blue solid curves denote the median Dst index (with an inverted scale to the right), while blue dashed curves denote the 25% and 75% quantiles

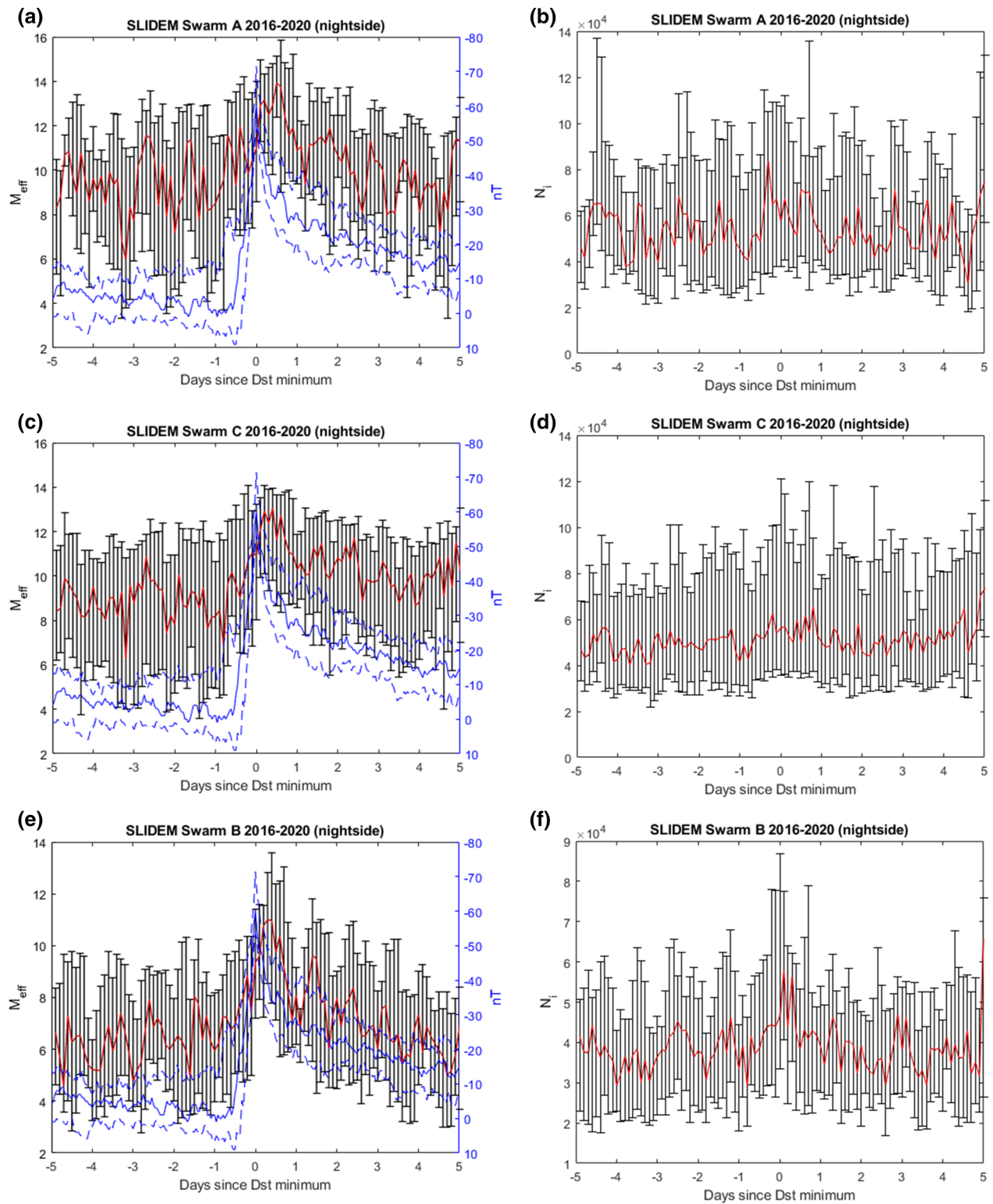


**Fig. 3** As Fig. 2 but for the nightside. Superposed epoch analysis of nightside effective ion mass (left) and density (right) for Swarm A (top), C (middle) and B (bottom), for the years specified in the panel titles. **a**, **c** and **e** show the effective ion mass for Swarm A, Swarm C and Swarm B respectively, while **b**, **d** and **f** show the ion density for the same spacecraft. The plots show the median values (red), while error bars denote the upper and lower quartiles. Blue solid curves denote the median Dst index (with an inverted scale to the right), while blue dashed curves denote the 25% and 75% quantiles.

would be at Point Arguello, California, while local noon would be at Dhaifra, UAE. Stations near the magnetic equator were avoided in order to try and minimize the effects of phenomena such as Equatorial Spread-F (e.g., Szuszczewicz et al. 1981). Likewise, stations located in the auroral zone were avoided since the Swarm effective mass product becomes invalid at those latitudes. A list of the selected stations for each storm can be found in Additional file 1: Table S2. Once the suitable stations were selected, for the time corresponding to as close as possible to the hour of the Dst minimum, the hmF2 and f0F2 readings were taken. Such hmF2 and f0F2 readings were also taken for up to  $-5$  days from zero epoch, as well as up to  $+5$  days from zero epoch. This approach makes it possible to observe hmF2 and f0F2 (and thus, NmF2) evolution with storm time in the same way as with Swarm data. In total, out of the 39 storm events, 22 dayside and 31 nightside events had

valid ground station data coverage. The obtained statistical results, in the form of medians and quartiles, are displayed in Fig. 4. It can be seen that, in agreement with the results inferred from Swarm data, hmF2 rises during storm times both on the dayside and the nightside by  $\sim 50$ – $60$  km compared to its pre-storm values. In addition, small storm-time increases in electron density (NmF2) are also observed, which are again in agreement with Swarm SLIDEM results. Note however that the error bars for the density are larger compared with the hmF2 results, suggesting that it is not possible to obtain statistically significant results from this data regarding storm-time NmF2 changes. For hmF2, on the other hand, there is a clear storm-time increase, with the F2-layer peak moving upwards by  $\sim 50$ – $60$  km relative to its pre-storm values, and returning close to its pre-storm values  $\sim 2$  days after the Dst minimum.

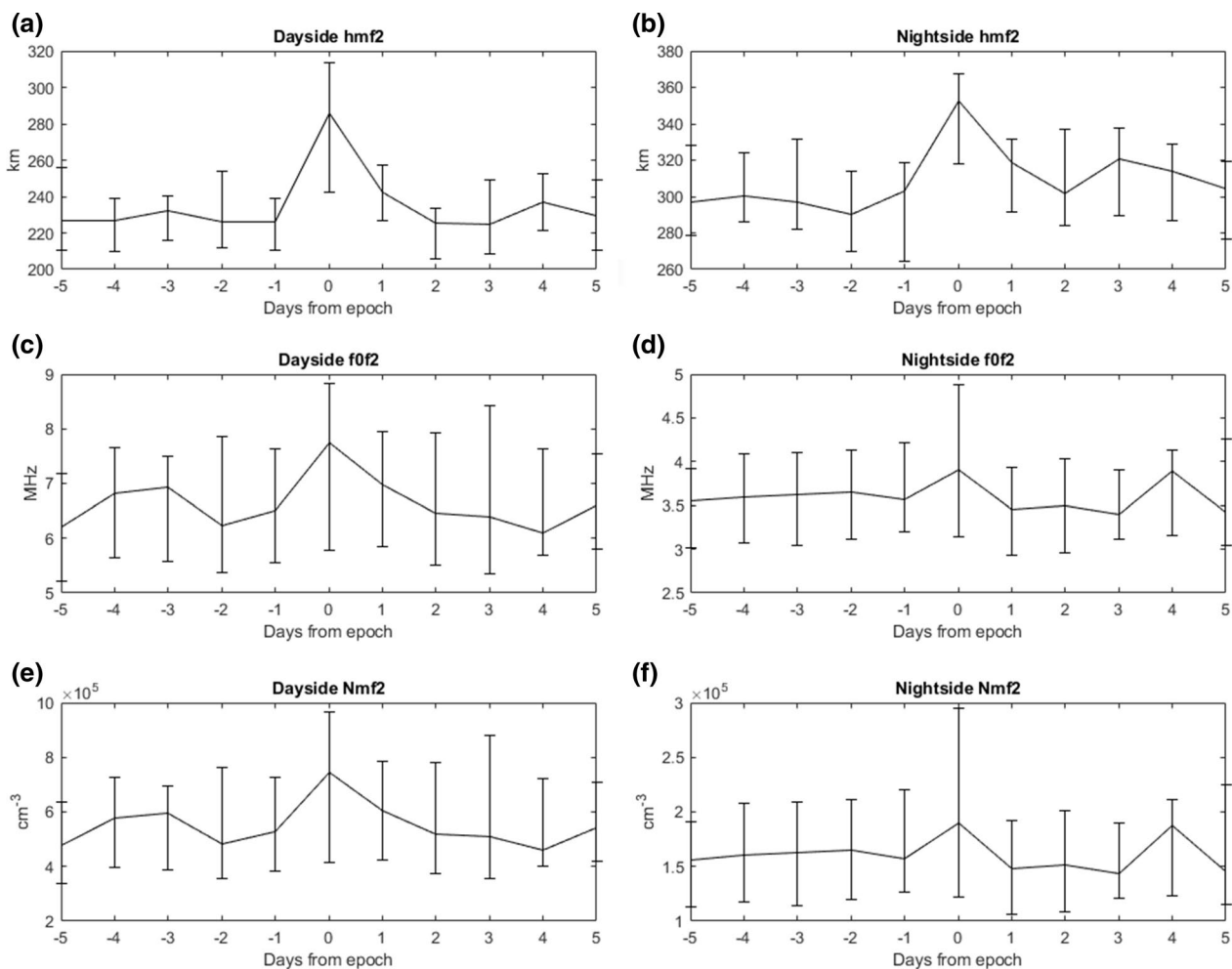


**Fig. 4** Statistical results based on ionosonde data for the same set of storms as was utilized for the Swarm SLIDEM analysis, and where appropriate ionosonde data were available. Panels **a**, **b** show the storm-time hmF2 evolution, panels **c**, **d** show the evolution in f0F2 and panels **e**, **f** show NmF2 calculated using Eq. (2). The plots show the median values, while the upper and lower error bars denote the 25% and 75% quantiles, respectively

### Latitude dependence of effective mass dynamics

Taking advantage of Swarm's relatively short orbital period ( $\sim 90$  min), it is possible to observe the latitude dependence of any storm-time  $M_{\text{eff}}$  changes, to determine whether they originate from low or high latitudes. This in turn makes it possible to determine which physical mechanisms predominate in the storm-time vertical transport dynamics. In Fig. 5, an example storm time period (for the storm of 13 October 2016) is examined. Effective ion mass, SLIDEM ion density, as well as ion and electron temperatures derived from SITE (Lomidze et al. 2021) are displayed. In Fig. 5a it can be seen that, for the nightside storm-time changes in  $M_{\text{eff}}$  (top half of the plot, signified by lower  $M_{\text{eff}}$  values indicative of greater light ion abundances), both the main-phase  $M_{\text{eff}}$  enhancement and the later recovery-phase  $M_{\text{eff}}$  drop, appear to begin at higher latitudes first and with the changes then propagating equatorward. A density enhancement also appears around Dst minimum, both

on the dayside and the nightside. From Fig. 5c it can be seen that storm-time ion temperature undergoes a small increase on both the dayside and the nightside, starting at high latitudes and propagating equatorward. Finally, from Fig. 5d, it appears that storm-time dayside electron temperatures drop around Dst minimum, though their latitude dependence is hard to disentangle from diurnal variation. The dayside storm-time electron temperature drop in Fig. 5d appears to correspond with the density increase in Fig. 5b, in line with past literature (e.g., Su et al. 2015). There also appears to exist a small storm-time electron temperature increase on the nightside, similarly to the ion temperature increase. In all, it comprises evidence of localized heating, possibly initiated by, e.g., Joule heating processes at higher, auroral latitudes, which can be associated with latitude-dependent  $[O^+]$  fraction increase, as well as a storm-time increase in ion density, resulting in an enhanced ion-neutral frictional heating.

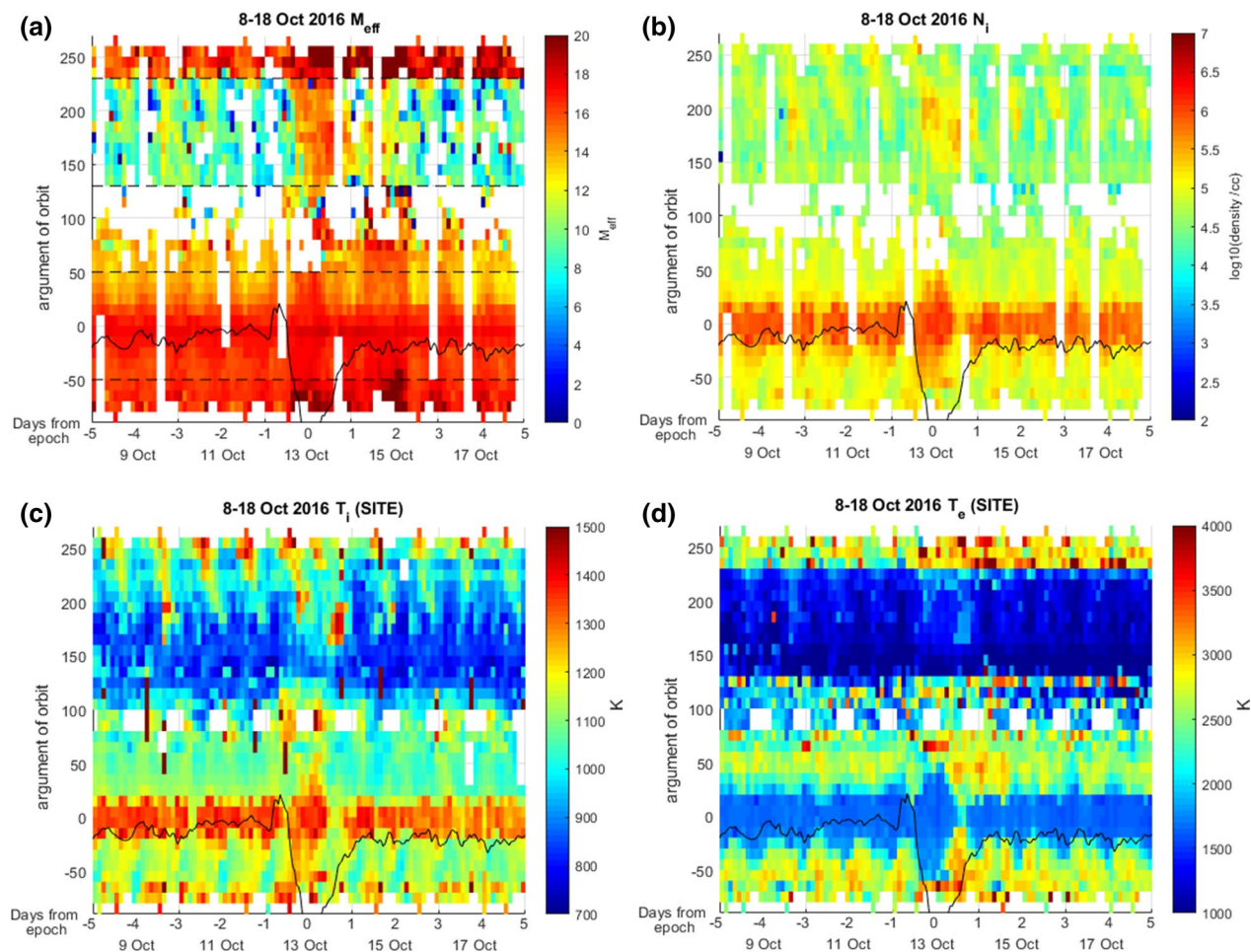


**Fig. 5** Plots for the 13 October 2016 storm, with Dst index overlotted in black. Panel **a** shows the effective ion mass, **b** shows the SLIDEM density, **c** shows the SITE ion temperature, while **d** shows the SITE electron temperature. Ascending MLT = 16, descending MLT = 4



## Discussion and conclusions

Using the superposed epoch analysis of the Swarm SLIDEM ion composition data, we found that the [O+] fraction in the topside ionosphere rapidly increases both on the dayside and nightside during storm times, beginning ~5–14 h before the Dst minimum and reaching its maximum values ~5–14 h after Dst minimum. Thereafter, it returns to pre-storm values over the next several days. At the same time, no significant global changes in ion or electron temperatures are observed, although localized temperature changes are evident in some individual events (Fig. 5). Small density increases are also observed around Dst minimum, though not as clearly as the effective ion mass increases.

The storm-time changes, observed in tandem on Swarm A/C and Swarm B, along with the absence of large-scale temperature changes, are indicative of an upward storm-time transport of the topside ionosphere, which begins after the SSC and reaches its maximum shortly after the Dst minimum. Thereafter, the topside ionosphere returns to its pre-storm height. This uplifting is believed to be caused by two candidate mechanisms (e.g., Prölss 1995; Rishbeth et al. 1998; Namgaladze et al. 2000): high-latitude heating leading to neutral thermospheric winds propagating equatorward and lifting the F2 layer, and/or the increased storm-time electric fields (prompt penetration electric field (PPEF) on short timescales, and disturbance dynamo electric fields (DDEF) on longer timescales), leading to upward  $E \times B$  drift. Prölss (1995) argues that these two mechanisms will have different latitude dependence, i.e., the thermospheric winds will cause the F2-layer to rise first at higher latitudes, then at lower latitudes, whereas the  $E \times B$  drift of the prompt penetration E-fields will cause the rise at lower latitudes first, then at higher latitudes. From Fig. 5, it appears in that event, on the nightside, the increased [O+] fraction is observed at higher latitudes first, propagating to lower latitudes. This suggests that in this case, thermospheric winds are the cause. A more comprehensive statistical study of the latitude dependence of the F2-layer rise and fall is left for a future study.

These results are in agreement with recent studies by Kotov et al. (2019) and Reznichenko (2021) who used the Kharkiv ISR data to investigate the [H+] fraction during small geomagnetic storms. The authors likewise report on the rise of hmF2 during storm times, while observing no major changes in plasma temperatures, in line with our observations.

It can be inferred from Figs. 2 and 3 that, since the storm-time  $M_{\text{eff}}$  values on Swarm B rise above pre-storm values on Swarm A and C, that the storm-time [H+]/[O+] transition height moves upwards by at least ~70 km (the vertical separation distance between Swarm A/C

and Swarm B orbits) on the timescale of hours. This is true for both the dayside and nightside. This result, as well as the increases in storm-time density, is consistent with earlier findings by Huang et al. (2005) who observed the F-region peak rising by ~80 km during storm time. Timoçin (2022) likewise reported on density changes observed by Swarm during storm times, which were interpreted as being due to PPEF influence.

Ground-based ionosonde data were utilized as independent measurements to confirm that the dynamics observed by Swarm are consistent with vertical plasma transport. Indeed, our analysis suggests that this appears to be the case as the ionosonde data show clear storm-time upward motion of hmF2 (Fig. 4) for the same storms as were studied in the Swarm SLIDEM analysis. The upward motion of ~50–60 km is consistent with the vertical motion of ~70–80 km inferred from the Swarm data. The slightly higher Swarm values may be due to the fact that the maximum F2-layer heights do not occur exactly at Dst minimum, but in general some hours after it (see Figs. 2, 3). Another possibility is bias in either the Swarm SLIDEM measurements and/or the ground ionosondes with inferring hmF2.

For NmF2, the results are less clear, although it does show evidence of storm-time increases on average. Interestingly, the nightside NmF2 storm-time increases observed by ionosondes are less clear than for the dayside. It is known that both positive and negative F-layer storms exist (e.g., Rishbeth et al. 1998) and that main- and recovery-phase density dynamics can be opposite on opposing MLT sectors, i.e., a main-phase density increase at noon can correspond to a main-phase density decrease at midnight (Timoçin 2022). From the dataset selected for this study it is not possible to tell whether the observed evidence of storm-time density increases points to the fact that there are more positive storms than negative storms, or whether the positive storm density increases are simply larger (or more often) for this particular dataset.

It is not possible to unambiguously determine the individual ion composition from  $M_{\text{eff}}$  when more than two ion species are present. We nevertheless assume a 2-species plasma on the dayside to gain insight into the role of light ions relative to heavier ions at the altitude of the satellite. This was done also, for example, by Park (2022). This assumption is justified since [H+] is the lightest ion, and therefore the one which disproportionately affects the effective mass parameter, while [O+] is by far the most abundant. Minor ions such as [He+], [N+] and [NO+] only have a minor influence on effective mass under most conditions encountered in a realistic ionosphere. Additional file 1: Fig. S3 demonstrates the control of effective mass by [H+] under various

theoretical minor ion abundances. At Swarm A/C heights ( $\sim 450$  km), the quiet-time dayside ionosphere with  $M_{\text{eff}} \sim 14$  AMU would correspond to  $\sim 1\%$  H $^{+}$  and  $99\%$  O $^{+}$ , which changes to virtually  $100\%$  O $^{+}$  during storm times. Meanwhile at Swarm B height ( $\sim 520$  km), the quiet-time  $M_{\text{eff}} \sim 12$  AMU maps to  $\sim 2\%$  H $^{+}$ , which falls to  $> 1\%$  H $^{+}$  during storm times. If we apply the same approach to the nightside, on Swarm A/C the H $^{+}$  fraction would fall from  $\sim 5$  to  $\sim 2\%$  during storm times, while on Swarm B the H $^{+}$  fraction would drop from  $\sim 11$  to  $\sim 5\%$ .

Dayside latitude dependence of effective ion mass is unclear. Although there is some evidence for  $M_{\text{eff}}$  changes beginning at high latitudes and propagating to lower latitudes, it is not symmetric across hemispheres, with dayside northern hemisphere values exhibiting lower  $M_{\text{eff}}$  values than southern hemisphere during the event in Fig. 5. The origin of this phenomenon is currently unknown, and it may be due to instrumental effects, such as photoelectron current. Until this is resolved, we believe it may not be prudent to draw conclusions on latitude dependence on the dayside. This does not affect the superposed epoch results, since the  $M_{\text{eff}}$  values for Figs. 2 and 3 are obtained from those averaged over the entire domain  $\pm 50$  deg QDlat, i.e., over both the northern and southern hemispheres. Statistical effective mass responses to storm times as a function of hemisphere are included in Additional file 1: Fig. S4.

The storm-time vertical motion of the topside ionosphere, and its associated effective mass signature observed by Swarm, may make it possible to empirically infer both hmF2 and f0F2 (the critical frequency of the ionospheric F2 layer, which is a function of electron density) from SLIDEM data. These parameters are of crucial importance in high-frequency (HF) radio propagation (e.g., Rush et al. 1974; Fagre et al. 2019). This study is left for future follow-up work. As evidenced in Fig. 1, it is not possible to capture these rapid storm-time changes of plasma ion composition using IRI or similar empirical models, and so their observation using Swarm may provide a timely and high-resolution estimation of these critical parameters.

## Supplementary Information

The online version contains supplementary material available at <https://doi.org/10.1186/s40623-023-01818-3>.

**Additional file 1. Fig. S1:** For Swarm A, C, and B, superposed epoch statistics of SITE ion temperatures (a, b, c, respectively) and electron temperatures (d, e, f, respectively). Solid line denotes the median values, while the error bars denote the 25% and 75% quartiles. **Table S2:** Ionosonde HmF2 and f0F2 values for the same geomagnetic storms dataset as used to generate the Swarm plots. Every 11-row section denotes a storm, with the middle row denoting the day and hour of the storm (zero epoch) while the 5 rows above and below it denote the 5 days above and below the storm, respectively. **Fig. S3:** A graph demonstrating the control of

effective mass by the [H $^{+}$ ] fraction under various concentrations of [He $^{+}$ ], [N $^{+}$ ], [O $^{+}$ ] and [NO $^{+}$ ]. **Fig. S4:** Effective mass superposed epoch statistics highlighting hemispheric differences. Blue plots denote  $M_{\text{eff}}$  statistics in the northern hemisphere, red show the southern hemisphere, and pink shows equatorial latitudes.

## Acknowledgements

The authors acknowledge helpful discussions with S. Buchert, N. Olsen, and C. Stolle. This paper uses ionospheric data from the USAF NEXION Digisonde network, the NEXION Program Manager is Annette Parsons. Data from the Brazilian Ionosonde network are made available through the EMBRACE program from the National Institute for Space Research (INPE). This publication uses data from the ionospheric observatory in Dourbes, owned and operated by the Royal Meteorological Institute (RMI) of Belgium. This publication makes use of data from Ionosonde stations, owned by Institute of Geology and Geophysics, Chinese Academy of Sciences (IGGCAS) and supported in part by Solar-Terrestrial Environment Research Network of CAS and Meridian Project of China.

## Author contributions

IPP conceived the study, performed the analysis, and wrote the paper. JKB, MF and LL assisted in developing the methodology and interpreting the results. All authors read and approved the final manuscript.

## Funding

IPP and MF were supported by the European Space Agency Swarm DISC SLIDEM contract from DTU Space. JKB was supported by funding from the Canadian Space Agency. LL is in part supported by Canadian Space Agency Grant 21SUSTSHLE.

## Availability of data and materials

Swarm SLIDEM data are available from ESA at [https://swarm-diss.eo.esa.int/#swarm%2FAdvanced%2FPlasma\\_Data%2F2\\_Hz\\_Ion\\_Drift\\_Density\\_and\\_Effective\\_Mass\\_dataset](https://swarm-diss.eo.esa.int/#swarm%2FAdvanced%2FPlasma_Data%2F2_Hz_Ion_Drift_Density_and_Effective_Mass_dataset). Geomagnetic indices including Dst index may be found at <https://omniweb.gsfc.nasa.gov> using the browser. The ionosonde data for the individual stations may be accessed at: <https://lgdc.uml.edu/common/DIDBFastStationList>

## Declarations

## Competing interests

The authors declare that they have no competing interests.

Received: 2 December 2022 Accepted: 10 April 2023

Published online: 24 April 2023

## References

- Balan N, Liu LB, Le HJ (2018) A brief review of equatorial ionization anomaly and ionospheric irregularities. *Earth Planet Phys* 2(4):257–275. <https://doi.org/10.26464/epp2018025>
- Bilitza D, Xiong C (2021) A solar activity correction term for the IRI topside electron density model. *Adv Space Res* 68:2124–2137. <https://doi.org/10.1016/j.asr.2020.11.012>
- Bilitza D, Altadill D, Truhlik V, Shubin V, Galkin I, Reinisch B, Huang X (2017) International reference ionosphere 2016: from ionospheric climate to real-time weather predictions. *Space Weather* 15:418–429. <https://doi.org/10.1002/2016SW001593>
- Billett DD, McWilliams KA, Pakhotin IP, Burchill JK, Knudsen DJ, Martin CJ (2022) High-resolution Poynting flux statistics from the Swarm mission: How much is being underestimated at larger scales? *J Geophys Res Space Phys* 127:e2022JA030573. <https://doi.org/10.1029/2022JA030573>
- Carpenter D, Lemaire J (1997) Erosion and recovery of the plasmasphere in the plasmopause region. *Space Sci Rev* 80:153–179. <https://doi.org/10.1023/A:1004981919827>

- Chappell CR (1982) Initial observations of thermal plasma composition and energetics from dynamics explorer-1. *Geophys Res Lett* 9(9):929–932. <https://doi.org/10.1029/GL009i009p00929>
- Fagre M, Zossi BS, Chum J, Yigit E, Elias AG (2019) Ionospheric high frequency wave propagation using different IRI hmF2 and foF2 models. *J Atmos Sol-Terr Phys* 196:105141
- Friis-Christensen E, Lühr H, Knudsen D, Haugmans R (2008) Swarm—an Earth observation mission investigating geospace. *Adv Space Res* 41(1):210–216. <https://doi.org/10.1016/j.asr.2006.10.008>
- Gallagher DL, Comfort RH, Katus RM, Sandel BR, Fung SF, Adrian ML (2021) The breathing plasmasphere: erosion and refilling. *J Geophys Res Space Phys* 126:e2020JA028727. <https://doi.org/10.1029/2020JA028727>
- Huang C-S, Foster JC, Goncharenko LP, Erickson PJ, Rideout W, Coster AJ (2005) A strong positive phase of ionospheric storms observed by the Millstone Hill incoherent scatter radar and global GPS network. *J Geophys Res* 110:A06303. <https://doi.org/10.1029/2004JA010865>
- Hussain S, Marchand R (2014) Sheath-induced distortions in particle distributions near enhanced polar outflow probe particle sensors. *Phys Plasmas* 21(7):072902. <https://doi.org/10.1063/1.4887257>
- Kim E-H, Johnson JR (2016) Full-wave modeling of EMIC waves near the He<sup>+</sup> gyrofrequency. *Geophys Res Lett* 43(1):13–21. <https://doi.org/10.1002/2015GL066978>
- King JH, Papitashvili NE (2005) Solar wind spatial scales in and comparisons of hourly wind and ACE plasma and magnetic field data. *J Geophys Res* 110:A02104. <https://doi.org/10.1029/2004JA010649>
- Knudsen DJ, Kelley MC, Vickrey JF (1992) Alfvén waves in the auroral ionosphere: a numerical model compared with measurements. *J Geophys Res* 97:77–90. <https://doi.org/10.1029/91JA02300>
- Knudsen DJ, Burchill JK, Buchert SC, Eriksson AI, Gill R, Wahlund JE et al (2017) Thermal ion imagers and Langmuir probes in the Swarm electric field instruments. *J Geophys Res Space Phys* 122:2655–2673. <https://doi.org/10.1002/2016JA022571>
- Kotov DV, Richards PG, Truhlik V, Bogomaz OV, Shulha MO, Maruyama N et al (2018) Coincident observations by the Kharkiv IS radar and ionosonde, DMSP and Arase (ERG) satellites, and FLIP model simulations: implications for the NRLMSISE-00 hydrogen density, plasmasphere, and ionosphere. *Geophys Res Lett* 45:8062–8071. <https://doi.org/10.1029/2018GL079206>
- Kotov DV, Richards PG, Truhlik V, Maruyama N, Fedrizzi M, Shulha MO et al (2019) Weak magnetic storms can modulate ionosphere-plasmasphere interaction significantly: mechanisms and manifestations at mid-latitudes. *J Geophys Res Space Phys* 124:9665–9675. <https://doi.org/10.1029/2019JA027076>
- Krall J, Emmert JT, Sassi F, McDonald SE, Huba JD (2016) Day-to-day variability in the thermosphere and its impact on plasmasphere refilling. *J Geophys Res Space Phys* 121:6889–6900. <https://doi.org/10.1002/2015JA022328>
- Lomidze L, Burchill JK, Knudsen DJ, Huba JD (2021) Estimation of ion temperature in the upper ionosphere along the Swarm satellite orbits. *Earth Space Sci*. <https://doi.org/10.1029/2021EA001925>
- Lysak RL (1991) Feedback instability of the ionospheric resonant cavity. *J Geophys Res* 96:1553–1568. <https://doi.org/10.1029/90JA02154>
- Marchand R, Hussain S (2015) Aberrations in particle distribution functions near e-POP particle sensors. *IEEE Trans Plasma Sci* 43(9):2776–2781. <https://doi.org/10.1109/TPS.2015.2428715>
- Namgaladze AA, Förster M, Yurik RY (2000) Analysis of the positive ionospheric response to a moderate geomagnetic storm using a global numerical model. *Ann Geophys* 18:461–477
- Nosé M, Matsuoka A, Kumamoto A et al (2020) Oxygen torus and its coincidence with EMIC wave in the deep inner magnetosphere: Van Allen Probe B and Arase observations. *Earth Planets Space* 72:111. <https://doi.org/10.1186/s40623-020-01235-w>
- Pakhotin IP, Mann IR, Lysak RL, Knudsen DJ, Gjerloev JW, Rae IJ, Balasis G (2018) Diagnosing the role of Alfvén waves in magnetosphere–ionosphere coupling: swarm observations of large amplitude nonstationary magnetic perturbations during an interval of northward IMF. *J Geophys Res Space Phys*. <https://doi.org/10.1002/2017JA024713>
- Pakhotin IP, Mann IR, Knudsen DJ, Lysak RL, Burchill JK (2020) Diagnosing the role of Alfvén waves in global field-aligned current system dynamics during southward IMF: swarm observations. *J Geophys Res Space Phys* 125:e2019JA027277. <https://doi.org/10.1029/2019JA027277>
- Pakhotin IP, Mann IR, Xie K et al (2021) Northern preference for terrestrial electromagnetic energy input from space weather. *Nat Commun* 12:199. <https://doi.org/10.1038/s41467-020-20450-3>
- Pakhotin IP, Burchill JK, Förster M et al (2022a) The Swarm Langmuir probe ion drift, density and effective mass (SLIDEM) product. *Earth Planets Space* 74:109. <https://doi.org/10.1186/s40623-022-01668-5>
- Pakhotin IP, Mann IR, Sydorenko D, Rankin R (2022b) Novel EMIC wave propagation pathway through Buchsbaum resonance and interhemispheric wave interference: swarm observations and modeling. *Geophys Res Lett* 49:e2022bGL098249. <https://doi.org/10.1029/2022GL098249>
- Park J (2022) Ratio between oversatellite electron content and plasma density measured by Swarm: a proxy for topside scale height. *J Geophys Res Space Phys* 127:e2021JA030137. <https://doi.org/10.1029/2021JA030137>
- Prölss GW (1995) Ionospheric F-region storms. In: Volland H (ed) *Handbook of atmospheric electrodynamics*, vol 2. CRC Press, Boca Raton, pp 195–248
- Reinisch BW, Galkin IA (2011) Global ionospheric radio observatory (GIRO). *Earth Planet Space* 63:377–381. <https://doi.org/10.5047/eps.2011.03.001>
- Reznichenko MO (2021) Manifestations of weak space weather variations in the ionosphere-plasmasphere system: results of observations and simulations. Thesis, Kharkiv Polytechnic Institute. <http://repository.kpi.kharkov.ua/handle/KhPI-Press/55322>
- Rishbeth H (1998) How the thermospheric circulation affects the ionospheric F2-layer. *J Atmos Solar-Terr Phys* 60:1385–1402
- Rishbeth H, Fuller-Rowell TJ, Rees D (1987) Diffusive equilibrium and vertical motion in the thermosphere during a severe magnetic storm: a computational study. *Planet Space Sci* 35:1157–1165
- Rush CM, Miller D, Gibbs J (1974) The relative daily variability of foF2 and hmF2 and their implications for hf Radio propagation. *Radio Sci* 9(8–9):749–756. <https://doi.org/10.1029/RS009i008p00749>
- Shprits YY, Subbotin DA, Meredith NP, Elkington SR (2008) Review of modeling of losses and sources of relativistic electrons in the outer radiation belt II: local acceleration and loss. *J Atmos Solar Terr Phys* 70:1694–1713. <https://doi.org/10.1016/j.jastp.2008.06.014>
- Su F, Wang W, Burns AG, Yue X, Zhu F (2015) The correlation between electron temperature and density in the topside ionosphere during 2006–2009. *J Geophys Res Space Phys* 120:10724–10739. <https://doi.org/10.1002/2015JA021303>
- Szuszczewicz EP, Singh M, Holmes JC (1981) Satellite and rocket observations of equatorial spread-F irregularities: a two-dimensional model. *J Atmos Terr Phys* 43(8):779–784. [https://doi.org/10.1016/0021-9169\(81\)90054-4](https://doi.org/10.1016/0021-9169(81)90054-4)
- Timofin E (2022) Swarm satellite observations of the effect of prompt penetration electric fields (PPEFs) on plasma density around noon and midnight side of low latitudes during the 07–08 September 2017 geomagnetic storm. *Adv Space Res* 69:1335–1343. <https://doi.org/10.1016/j.asr.2021.11.027>
- Truhlik V, Bilítza D, Trisková L (2015) Towards better description of solar activity variations in IRI ion composition model. *Adv Space Res* 55(8):2099–2105. <https://doi.org/10.1016/j.asr.2014.07.033>
- Xiong C, Jiang H, Yan R, Lühr H, Stolle C, Yin F et al (2022) Solar flux influence on the in-situ plasma density at topside ionosphere measured by Swarm satellites. *J Geophys Res Space Phys* 127:e2022JA030275. <https://doi.org/10.1029/2022JA030275>
- Yau AW, André M (1997) Sources of ion outflow in the high latitude ionosphere. *Space Sci Rev* 80:1–25. <https://doi.org/10.1023/A:1004947203046>
- Yau AW, James HG (2015) CASSIOPE enhanced polar outflow probe (e-POP) mission overview. *Space Sci Rev* 189(1–4):3–14. <https://doi.org/10.1007/s11214-015-0135-1>

## Publisher's Note

Springer Nature remains neutral with regard to jurisdictional claims in published maps and institutional affiliations.